Origins of the extragalactic background at 1 mm from a combined analysis of the AzTEC and MAMBO data in GOODS-N

Kyle Penner,[1]* Alexandra Pope,[2]† Edward L. Chapin,[3] Thomas R. Greve,[4,5] Frank Bertoldi,[6] Mark Brodwin,[7]‡ Ranga-Ram Chary,[8] Christopher J. Conselice,[9] Kristen Coppin,[10] Mauro Giavalisco,[11] David H. Hughes,[12] Rob J. Ivison,[13,14] Thushara Perera,[15] Douglas Scott,[3] Kimberly Scott[16] and Grant Wilson[11]

[1] *Department of Astronomy, University of Arizona, 933 N. Cherry Ave., Tucson, AZ 85721, USA*
[2] *National Optical Astronomy Observatory, 950 N. Cherry Ave., Tucson AZ 85719, USA*
[3] *Dept. of Physics and Astronomy, University of British Columbia, 6224 Agricultural Road, Vancouver, B.C. V6T 1Z1, Canada*
[4] *Max-Planck Institute for Astronomy, Königstuhl 17, 69117 Heidelberg, Germany*
[5] *Dark Cosmology Centre, Juliane Maries Vej 30, 2100 Copenhagen Ø, Denmark*
[6] *Argelander Institute for Astronomy, University of Bonn, Auf dem Huegel 71, 53121 Bonn, Germany*
[7] *Harvard-Smithsonian Center for Astrophysics, 60 Garden Street, Cambridge, MA 02138, USA*
[8] *Spitzer Science Center, California Institute of Technology, Pasadena, CA 91125, USA*
[9] *School of Physics and Astronomy, University of Nottingham, Nottingham NG7 2RD, UK*
[10] *Institute for Computational Cosmology, Durham University, South Road, Durham DH1 3LE, UK*
[11] *Department of Astronomy, University of Massachusetts, Amherst, MA 01003, USA*
[12] *Instituto Nacional de Astrofísica, Óptica y Electrónica, Luis Enrique Erro No. 1, Tonantzintla, Puebla, C.P. 72840, Mexico*
[13] *UK Astronomy Technology Centre, Royal Observatory, Blackford Hill, Edinburgh EH9 3HJ, UK*
[14] *Institute for Astronomy, University of Edinburgh, Blackford Hill, Edinburgh EH9 3HJ, UK*
[15] *Department of Physics, Illinois Wesleyan University, Bloomington, IL 61701, USA*
[16] *Department of Physics and Astronomy, University of Pennsylvania, Philadelphia, PA 19104, USA*

27 December 2013

ABSTRACT

We present a study of the cosmic infrared background, which is a measure of the dust obscured activity in all galaxies in the Universe. We venture to isolate the galaxies responsible for the background at 1 mm; with spectroscopic and photometric redshifts we constrain the redshift distribution of these galaxies. We create a deep 1.16 mm map ($\sigma \sim 0.5$ mJy) by combining the AzTEC 1.1 mm and MAMBO 1.2 mm datasets in GOODS-N. This combined map contains 41 secure detections, 13 of which are new. By averaging the 1.16 mm flux densities of individually undetected galaxies with 24 μm flux densities $> 25\,\mu$Jy, we resolve 31–45 per cent of the 1.16 mm background. Repeating our analysis on the SCUBA 850 μm map, we resolve a higher percentage (40–64 per cent) of the 850 μm background. A majority of the background resolved (attributed to individual galaxies) at both wavelengths comes from galaxies at $z > 1.3$. If the ratio of the resolved submillimeter to millimeter background is applied to a reasonable scenario for the origins of the unresolved submillimeter background, 60–88 per cent of the total 1.16 mm background comes from galaxies at $z > 1.3$.

Key words: galaxies: evolution – galaxies: high-redshift – methods: statistical.

1 INTRODUCTION

The cosmic infrared background (CIB) is the total dust emission from all galaxies in the Universe. The contribution of galaxies to the background varies with redshift; this variation constrains the evolution over cosmic time of the output of dust obscured AGN activity and star formation.

* kpenner@as.arizona.edu
† *Spitzer* Fellow
‡ W. M. Keck Postdoctoral Fellow

Decomposing the background into individual galaxies provides constraints as a function of redshift on the processes important to galaxy evolution.

Models predict that a large fraction of the CIB at longer (sub)millimeter wavelengths comes from galaxies at high redshift (Gispert, Lagache, & Puget 2000). The main evidence is that the SED of the (sub)mm background is less steep than the SED of a representative (sub)mm galaxy; the shallow slope of the background can be due to high redshift galaxies, so that the peak of their infrared SED shifts to observed (sub)mm wavelengths (Lagache, Puget, & Dole 2005). In this paper we address the question: 'What galaxies are responsible for the CIB at $\lambda \sim 1\,\mathrm{mm}$, and what is their redshift distribution?'

It is difficult to individually detect a majority of the galaxies that contribute to the millimeter background, as maps are limited by confusion noise due to the large point spread functions of current mm telescopes. To resolve the $\sim 1\,\mathrm{mm}$ background, we rely on a stacking analysis of galaxies detected at other wavelengths. Stacking is the process of averaging the millimeter flux density of a large sample of galaxies *not* individually detected in a millimeter map; the desired result is a high significance detection of the 'external' sample as a whole (or in bins of flux density, redshift, etc.).

Stacking the (sub)mm flux density of galaxies is not a new methodology. Several studies seek to decompose the background at $850\,\mu\mathrm{m}$ by stacking on SCUBA maps (Wang et al. 2006; Dye et al. 2006; Serjeant et al. 2008). These studies agree that the $850\,\mu\mathrm{m}$ background is not completely resolved by current samples of galaxies; however, they reach contradictory conclusions on the redshift distribution of the galaxies that contribute to the resolved background. Recently, stacking has been carried out on BLAST maps at 250, 350, and $500\,\mu\mathrm{m}$ (Marsden et al. 2009; Devlin et al. 2009; Pascale et al. 2009; Chary & Pope 2010). As with stacking on any map with a large PSF, stacking on BLAST maps is subject to complications when the galaxies are angularly clustered. We take this issue into consideration in our analysis in this paper.

We combine the AzTEC 1.1 mm (Perera et al. 2008) and MAMBO 1.2 mm (Greve et al. 2008) maps in the GOODS-N field to create a deeper map at an effective wavelength of 1.16 mm. A significant advantage of the combined 1.16 mm map over the individual 1.1 mm and 1.2 mm maps is reduced noise. We investigate the contribution of galaxies with $24\,\mu\mathrm{m}$ emission to the 1.16 mm background as a function of redshift. By stacking the same sample of galaxies on the SCUBA $850\,\mu\mathrm{m}$ map in GOODS-N, we calculate the relative contribution of galaxies to the background at $850\,\mu\mathrm{m}$ and 1.16 mm as a function of redshift; we use this to infer the redshift distribution of the galaxies contributing to the remaining, unresolved 1.16 mm background.

This paper is organized as follows: in §2, we describe the data and our analysis of the data; in §3 we describe stacking and several considerations when performing a stacking analysis. We present our results in §4, and conclude in §5.

2   DATA

2.1   Creating the combined 1.16 mm map

There are two deep millimeter surveys of the Great Observatories Origins Deep Survey North region (GOODS-N; Dickinson et al. 2003). The AzTEC survey at 1.1 mm carried out on the JCMT (PSF FWHM = 19.5 arcsec) reaches a 1σ depth of 0.96 mJy over $0.068\ \mathrm{deg}^2$ (Perera et al. 2008). The MAMBO survey at 1.2 mm carried out on the IRAM 30-m telescope (PSF FWHM = 11.1 arcsec) reaches a 1σ depth of 0.7 mJy over $0.080\ \mathrm{deg}^2$ (Greve et al. 2008). The noise values refer to the uncertainty in determining the flux density of a point source. For more details on the individual maps, we refer the reader to those papers.

We create a combined mm map from a weighted average of the AzTEC 1.1 mm and MAMBO 1.2 mm maps. We use the PSF-convolved maps that are on the same RA and Dec grid with the same pixel size ($2\,\mathrm{arcsec} \times 2\,\mathrm{arcsec}$).

The weighted average flux density in a pixel in the combined mm map is calculated as:

$$S_{\mathrm{measured}} = \frac{\frac{w_\mathrm{A} S_\mathrm{A}}{\sigma_\mathrm{A}^2} + \frac{w_\mathrm{M} S_\mathrm{M}}{\sigma_\mathrm{M}^2}}{\frac{w_\mathrm{A}}{\sigma_\mathrm{A}^2} + \frac{w_\mathrm{M}}{\sigma_\mathrm{M}^2}}, \tag{1}$$

where S_A and σ_A are the measured flux density and noise in the AzTEC 1.1 mm map, S_M and σ_M are the measured flux density and noise in the MAMBO 1.2 mm map, and the w's are constants.

The noise in each pixel from Eq. 1 is thus

$$\sigma = \frac{\sqrt{\frac{w_\mathrm{A}^2}{\sigma_\mathrm{A}^2} + \frac{w_\mathrm{M}^2}{\sigma_\mathrm{M}^2}}}{\frac{w_\mathrm{A}}{\sigma_\mathrm{A}^2} + \frac{w_\mathrm{M}}{\sigma_\mathrm{M}^2}}. \tag{2}$$

Use of the inverse variance weights in combining the two maps results in the map with minimum noise. We are instead interested in the resulting map with the *maximum* signal-to-noise ratio (SNR) of the sources, whether these sources are above or below some detection threshold. We introduce additional weights, w_A and w_M, which are constant multiplicative factors for the two individual maps. To rephrase the justification for these w's in astrophysical terms – at (sub)millimeter wavelengths, the spectral energy distributions (SEDs) of galaxies fall off $\propto \nu^{2+\beta}$ (a Rayleigh-Jeans fall off with emissivity index β); the flux density at 1.1 mm is higher than that at 1.2 mm. A simple inverse variance weighted average ($w_\mathrm{A} = w_\mathrm{M}$) does not account for this.

The optimal w's come from iteratively maximizing the SNR of the detections in the resulting combined map (in practice, we maximize the number of detections above 3.8σ). The two values are $[w_\mathrm{A}, w_\mathrm{M}] = [0.56, 0.44]$. Given these w's, the inverse variance weights, and that the transmission curves for the individual maps shown in Fig. 1 overlap, the central wavelength of the combined map is 1.16 mm. In the absence of *any* weighting, the combined map has an effective wavelength of 1.15 mm. Weighting the individual maps results in a small shift of the central wavelength of the combined map to 1.16 mm.

The combined 1.16 mm map has two significant advantages over the individual 1.1 mm and 1.2 mm maps: 1) reduced noise (by roughly $\sqrt{2}$); and 2) increased reliability of secure detections. The AzTEC and MAMBO cata-
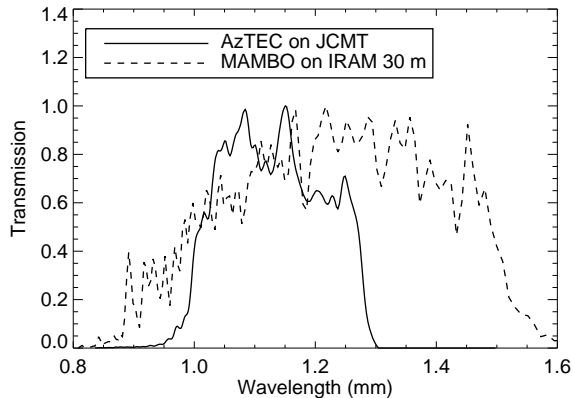
Figure 1. Transmission curves for the AzTEC and MAMBO detectors on their respective telescopes.

Figure 2. Distribution of normalized weights (Eq. 1) for pixels with $1\sigma < 1\,\mathrm{mJy}$ in the combined 1.16 mm map. The normalized weights applied to the AzTEC and MAMBO maps for each pixel sum to 1, so the histograms are symmetric about 0.5.

logues include some spurious detections (Perera et al. 2008; Greve et al. 2008); by combining the two (independent) maps, the secure detections in the resulting map may be more reliable (this is the expectation).

The penalties to pay for these advantages are that the FWHM of the PSF, and the effective wavelength, vary slightly across the 1.16 mm map. Alternatively, we could smooth the two individual raw maps to the same PSF resolution, at the expense of decreased SNR in each pixel. As the weights (defined as $w_\mathrm{A}/\sigma_\mathrm{A}^2$ and $w_\mathrm{M}/\sigma_\mathrm{M}^2$) change from pixel to pixel, we average different proportions of AzTEC 1.1 mm and MAMBO 1.2 mm flux densities. Fig. 2 shows the distributions of normalized weights (defined in the legend) from Eq. 1 for pixels with $1\sigma < 1\,\mathrm{mJy}$ in the combined 1.16 mm map. The majority of pixels in the combined map are in a small range of normalized weights (~ 0.4 for the AzTEC map, ~ 0.6 for the MAMBO map); the variation in FWHM and effective wavelength is small. The central wavelength of the combined map is calculated using these normalized weights and the quoted wavelengths of the two individual maps. The distribution of stacked flux densities for randomly chosen pixels in the combined map has zero mean, as expected based on the individual maps (§3).

The area in our combined 1.16 mm map with $1\sigma < 1\,\mathrm{mJy}$ is $0.082\,\mathrm{deg}^2$. We use the overlap between this region and the area covered by the $24\,\mu\mathrm{m}$ sources ($0.068\,\mathrm{deg}^2$) for the stacking analysis. While we focus on stacking using the combined 1.16 mm map due to its uniform depth (reaching $1\sigma \sim 0.5\,\mathrm{mJy}$), we also compare the stacking results using the SCUBA $850\,\mu\mathrm{m}$ survey of the GOODS-N region. The cleaned (of secure detections) $850\,\mu\mathrm{m}$ map (Pope et al. 2005) has a non-uniform, non-contiguous $0.031\,\mathrm{deg}^2$ area with $0.5 < 1\sigma < 5\,\mathrm{mJy}$. We ensure that both the clean and full SCUBA maps have a mean flux density of 0 mJy in the area with $24\,\mu\mathrm{m}$ sources.

Our terminology is as follows: *map* refers to a map convolved with its PSF, except when prefaced with 'raw'; *secure detections* are directly detected sources in the mm map – that is, non-spurious sources in the AzTEC 1.1 mm and MAMBO 1.2 mm maps, and sources with SNR ≥ 3.8 in the combined 1.16 mm map (see §2.2 for a justification of this threshold); hereafter, when we use the word *sources* we mean sources in an external catalogue that are not detected in the
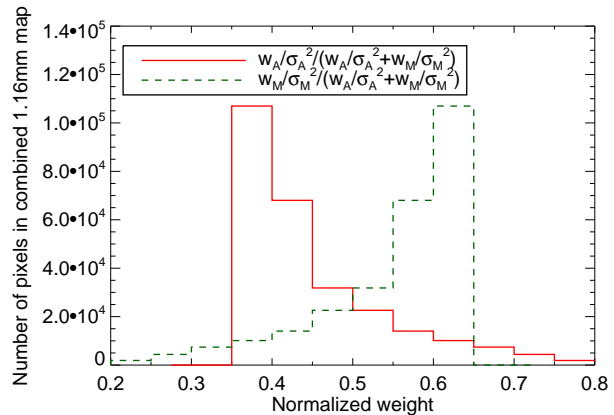
mm maps. A *cleaned* map has all secure detections subtracted before convolution with the PSF (§3.2), whereas a *full* map contains the secure detections.

The combined 1.16 mm map is publicly available at http://www.astro.umass.edu/∼pope/goodsn_mm/.

2.2 Verifying the 1.16 mm map

Detections in the combined 1.16 mm map are found by searching for peaks in the SNR map. As the SNR threshold is decreased, there is an increasing probability that some detections are spurious. Perera et al. (2008) and Greve et al. (2008) determine which detections, in their AzTEC 1.1 mm and MAMBO 1.2 mm maps, are most likely spurious; most spurious detections have SNR (before deboosting) < 3.8, and only 5 secure detections have SNR (before deboosting) < 3.8. We use this SNR threshold to make our secure detection list for the combined map. Positions and measured flux densities of secure 1.16 mm detections are given in Table 1.

Flux boosting is an important issue for detections at low SNR thresholds, particularly when the differential counts distribution ($\mathrm{d}N/\mathrm{d}S$) is steep, so that it is more likely for a faint detection's flux density to scatter up than for a bright detection's flux density to scatter down. Flux deboosting is a statistical correction to the measured flux density of a secure detection (Hogg & Turner 1998). The deboosting correction relies on a a simulated map using a model of the differential counts distribution (see Coppin et al. 2005). A simulation of the 1.16 mm map is subject to large uncertainties because we do not have exact knowledge of the PSF, so we choose to deboost the flux densities of secure detections using an empirical approach.

To verify our method of combining the two maps, we want to compare the deboosted flux densities of secure detections in the 1.16 mm map with their deboosted flux densities in the 1.1 mm and 1.2 mm maps. Our approach to obtain empirically deboosted flux densities is to fit a function that relates the *deboosted* flux densities of secure detections in the 1.1 mm and 1.2 mm maps to the *measured* flux densities and noise values in those maps. We then use the derived formula to estimate empirically deboosted flux densities for

the secure 1.16 mm detections from the measured 1.16 mm flux densities and noises. We find

$$S_{\text{deboosted}} = 1.55\, S_{\text{measured}}^{0.89} - 2.7\, \sigma, \tag{3}$$

where S_{measured} and σ are in mJy. For the secure AzTEC 1.1 mm and MAMBO 1.2 mm detections, the residuals between the deboosted flux densities from this relation and the deboosted flux densities in Perera et al. (2008) and Greve et al. (2008) have a standard deviation of 0.1 mJy, an error well below the flux density noise values in all mm maps. This formula is only valid in the range of SNR covered by the AzTEC and MAMBO detections, so we do not deboost the flux density of source 1 (a 15σ source). Table 1 lists the deboosted flux densities for the secure 1.16 mm detections using this relation. For the main purposes of this paper, flux deboosting is not necessary since we stack the 1.16 mm flux densities of sources we know to exist from other observations.

Fig. 3 shows the comparison between deboosted flux densities for secure 1.16 mm and 1.1 mm detections. The combined 1.16 mm map recovers the majority of secure detections identified in the AzTEC 1.1 mm map – the arrows pointing down show that there are 4 secure detections in the AzTEC map that are not secure detections in the combined map.

Fig. 4 shows the comparison between deboosted flux densities for secure 1.16 mm and 1.2 mm detections. There are 14 secure detections in the MAMBO 1.2 mm map that are not coincident with secure detections in the combined 1.16 mm map (the down arrows in the right panel). However, the upper limits to the flux densities in the combined map are within the scatter about the solid line.

We conclude, based on the comparisons in Figs. 3 and 4, that our method of combining the AzTEC 1.1 mm and MAMBO 1.2 mm maps is effective. The combined 1.16 mm map has 13 new secure detections (Table 1); we do not expect the new detections to be in the individual maps.

2.3   GOODS-N MIPS 24 μm redshift catalog

Galaxies with detected 24 μm emission compose the most homogeneous set of dusty galaxies whose mm flux density can be stacked with significant results. We use the 24 μm catalogue from the GOODS-N *Spitzer*/MIPS survey, which has a uniform depth of $1\sigma \sim 5\,\mu$Jy in the regions of interest (Chary et al. in preparation); the 24 μm fluxes are measured at the positions of IRAC sources, so this catalogue pushes to faint 24 μm fluxes. We only stack $\geq 3\sigma$ 24 μm sources with $S_{24} > 25\,\mu$Jy. At flux densities above 50 μJy, the catalogue is 99 per cent complete; for $25 < S_{24} < 50\,\mu$Jy, the catalogue is 83 per cent complete (Magnelli et al. 2009). Completeness corrections to our results are negligible, so we do not apply them. We exclude sources that lie in the region of the 1.16 mm map with $1\sigma > 1$ mJy; in this region, the noise is non-uniform. The final 24 μm catalog for stacking has 2484 sources in 0.068 deg^2.

To decompose the contribution to the mm background from 24 μm sources as a function of redshift, we require either a photometric or spectroscopic redshift for each 24 μm source. We start by matching a source with a spectroscopic redshift from the catalogues of Barger, Cowie, & Wang (2008) and Stern et al. (in preparation) to each 24 μm source.

The match radius, 0.7 arcsec, is chosen by maximizing the number of unique matches while minimizing the number of multiple matches. We find spectroscopic redshifts for 1026 (41 per cent of the) 24 μm sources.

If no (or multiple) coincident sources with spectroscopic redshifts are found, we resort to the photometric redshift source catalogue of Brodwin et al. (in preparation) to find a source match. Photometric redshifts are constrained with deep $UBVRIzJK$ imaging, and provide redshift estimates for 872, or 35 per cent, of the 24 μm sources. Photometric redshift uncertainties are small compared to our redshift bins, since we are interested in the contribution to the background from galaxies in large redshift bins. If no (or multiple) coincident sources with photometric redshifts are found, we assign the 24 μm source to a 'redshift unknown' bin in the stacking analysis. Of the 2484 24 μm sources, 588 (24 per cent) have no spectroscopic or photometric redshift estimate available.

3   STACKING ANALYSIS

Our stacking procedure depends on two fundamental properties of the (sub)mm maps:

(1) *Every detection, and source, is a point source.* The PSFs are large; in all 3 maps the full-width-half-maxima (FWHM) are > 10 arcsec. This property has a number of implications. To make low SNR detection-finding easier, the raw maps are convolved with their PSFs; the result is a map where each pixel value is the flux density of a point source at the position of the pixel. Thus, to stack the millimeter flux densities of sources, we require only the values of single pixels in the map.

(2) *The means of the maps are 0 mJy.* These millimeter observations are taken, filtered, and reduced in such a way that the sum of all pixel values in the map is zero. In other words, the most likely value of a randomly chosen pixel is 0 mJy, a useful statistical property we explore in §3.1. However, the large PSF forces us to carefully consider the effects of having multiple sources clustered in the area covered by one PSF (also in §3.1).

Stacking is the process of averaging the flux density, at some wavelength (1.16 mm), of sources detected at another wavelength. To resolve the (sub)mm background, we want to stack a catalogue of sources whose emission correlates strongly with 1.16 mm emission, and we want this catalogue to have a large number of sources. A catalogue that meets these requirements has galaxies selected on dust emission at both low and high redshift. We do not expect a sample of stellar mass selected sources (for example, at 3.6 μm) to be efficient at isolating the galaxies responsible for the mm background, because 3.6 μm sources are a mix of dusty and non-dusty galaxies. The MIPS catalogue of 24 μm sources, though, is selected on dust emission to high redshift, and there is a known correlation between the flux densities at mid-infrared and far-infrared wavelengths (Chary & Elbaz 2001).

The stacking equation we use is similar to Eq. 1:

$$S_{\text{bin}} = \frac{\sum_{i=1}^{N_{\text{bin}}} \frac{S_{i,1.16}}{\sigma_{i,1.16}^2}}{\sum_{i=1}^{N_{\text{bin}}} \frac{1}{\sigma_{i,1.16}^2}}, \tag{4}$$
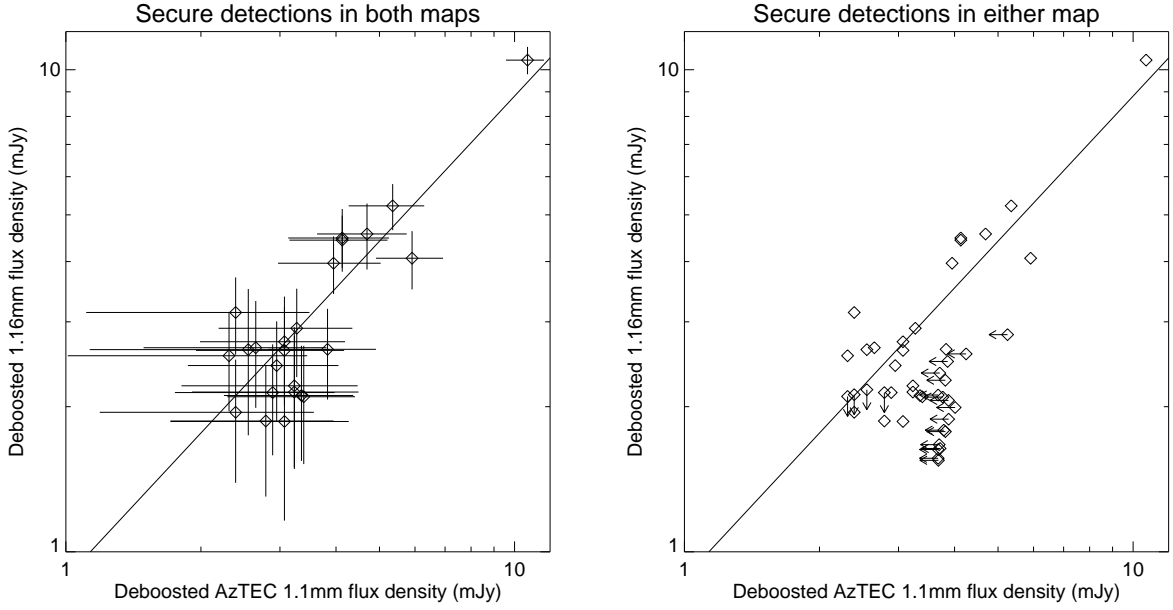
Figure 3. *Left panel*: Empirically deboosted combined 1.16 mm flux ($S_{\mathrm{deboosted}}$) as a function of deboosted AzTEC 1.1 mm flux ($S_{\mathrm{A,deboosted}}$) for detections which are secure in both maps. The solid line is the best-fitting line to the deboosted flux densities of secure detections ($S_{\mathrm{deboosted}} = 0.88 S_{\mathrm{A,deboosted}}$). *Right panel*: A comparison of deboosted flux densities for secure detections in either map. If a secure 1.16 mm detection does not coincide with a secure AzTEC 1.1 mm detection, a 3.8σ upper limit on the AzTEC 1.1 mm flux density is plotted. Similarly, if a secure AzTEC 1.1 mm detection does not coincide with a secure 1.16 mm detection, a 3.8σ upper limit on the 1.16 mm flux density is plotted.
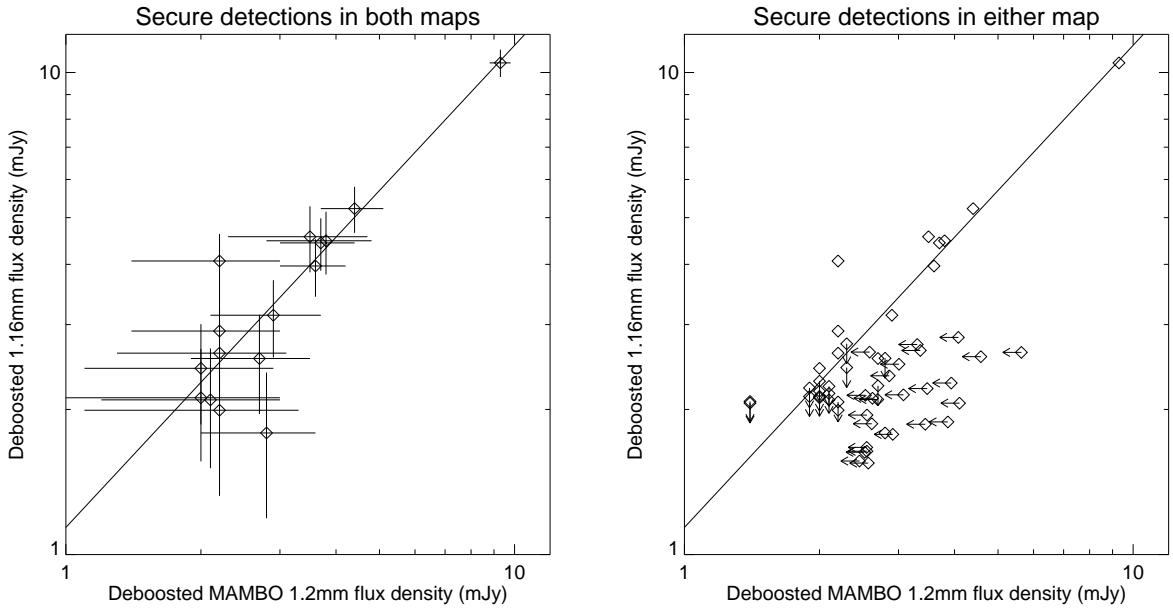

Figure 4. *Left panel*: Empirically deboosted combined 1.16 mm flux ($S_{\mathrm{deboosted}}$) as a function of deboosted MAMBO 1.2 mm flux ($S_{\mathrm{M,deboosted}}$) for detections which are secure in both maps. The solid line is the best-fitting line to the deboosted flux densities of secure detections ($S_{\mathrm{deboosted}} = 1.14 S_{\mathrm{M,deboosted}}$). *Right panel*: A comparison of deboosted flux densities for secure detections in either map. If a secure 1.16 mm detection does not coincide with a secure MAMBO 1.2 mm detection, a 3.8σ upper limit on the MAMBO 1.2 mm flux density is plotted. Similarly, if a secure MAMBO 1.2 mm detection does not coincide with a secure 1.16 mm detection, a 3.8σ upper limit on the 1.16 mm flux density is plotted. Based on this figure and Fig. 3, we conclude that our method of combining the AzTEC 1.1 mm and MAMBO 1.2 mm maps is valid.

Table 1. Secure detections in the combined 1.16 mm map (a weighted average of AzTEC 1.1 mm and MAMBO 1.2 mm maps).

Number	RA	Dec	S_{measured} mJy	σ mJy	SNR	$S_{\text{deboosted}}$ mJy	AzTEC ID	MAMBO ID
1	189.299114	62.369436	10.26	0.68	15.0	. . .	AzGN01	GN1200.1
2	189.137896	62.235510	5.24	0.57	9.1	5.2	AzGN03	GN1200.2
3	189.378717	62.216051	4.51	0.55	8.2	4.4	AzGN05	GN1200.4
4	189.297686	62.224436	4.09	0.54	7.6	3.9	AzGN07	GN1200.3
5	189.132927	62.286617	4.22	0.56	7.5	4.1	AzGN02	GN1200.13
6	189.112273	62.101043	4.81	0.67	7.2	4.5	AzGN06	GN1200.5
7	188.959560	62.178029	5.00	0.71	7.0	4.6	AzGN04	GN1200.12
8	189.308576	62.307210	3.46	0.57	6.1	3.1	AzGN26	GN1200.6
9	189.149018	62.119408	3.35	0.61	5.5	2.9	AzGN11	GN1200.14
10	189.190353	62.244432	3.02	0.56	5.4	2.6	AzGN08	. . .
11	188.973386	62.228058	3.10	0.60	5.1	2.6	AzGN13	GN1200.15
12	189.184207	62.327207	3.03	0.59	5.1	2.5	AzGN28	GN1200.9
13	189.138377	62.105511	3.31	0.66	5.0	2.7	AzGN12	. . .
14	189.213067	62.204995	2.88	0.57	5.0	2.4	AzGN14	GN1200.25
15	189.501924	62.269772	3.26	0.66	4.9	2.7	AzGN21	. . .
16	189.202112	62.351658	3.05	0.63	4.8	2.5	. . .	. . .
17	189.214098	62.339995	2.88	0.60	4.8	2.3	. . .	. . .
18	189.068612	62.254326	2.61	0.55	4.7	2.1	AzGN16	. . .
19	189.300036	62.203880	2.59	0.55	4.7	2.1	. . .	GN1200.29
20	189.114187	62.203822	2.61	0.57	4.6	2.1	AzGN10	. . .
21	189.407721	62.292688	2.62	0.58	4.5	2.1	AzGN09	. . .
22	189.400013	62.184363	2.63	0.58	4.5	2.1	. . .	GN1200.17
23	189.440268	62.148758	3.84	0.85	4.5	2.8	. . .	. . .
24	189.035270	62.244279	2.46	0.56	4.4	1.9	AzGN24	. . .
25	189.575648	62.241841	3.56	0.82	4.3	2.6	. . .	. . .
26	188.951634	62.257458	2.84	0.66	4.3	2.1	AzGN15	. . .
27	189.421566	62.206005	2.41	0.57	4.3	1.9	AzGN18	. . .
28	188.942743	62.192993	3.09	0.73	4.3	2.3	. . .	. . .
29	189.216774	62.083885	3.74	0.88	4.2	2.6	AzGN25	. . .
30	188.920762	62.242944	3.01	0.71	4.2	2.2	AzGN17	. . .
31	189.323691	62.133314	2.74	0.67	4.1	2.0	. . .	GN1200.23
32	189.033574	62.148164	2.42	0.60	4.0	1.8	. . .	GN1200.7
33	189.090016	62.268797	2.23	0.56	4.0	1.7	. . .	. . .
34	189.143551	62.322737	2.44	0.61	4.0	1.8	. . .	. . .
35	189.258342	62.214444	2.19	0.55	4.0	1.6	. . .	. . .
36	189.039961	62.255953	2.21	0.56	4.0	1.6	. . .	. . .
37	188.916328	62.212377	2.97	0.75	4.0	2.1	. . .	. . .
38	189.327507	62.231090	2.12	0.54	3.9	1.6	. . .	. . .
39	189.020746	62.114810	2.71	0.70	3.9	1.9	AzGN19	. . .
40	189.238057	62.279444	2.14	0.56	3.8	1.5	. . .	. . .
41	189.550659	62.248008	2.78	0.73	3.8	1.9	. . .	. . .

Columns: RA and Dec are in decimal degrees, and are reported from the centre of the pixel with maximum SNR ($S_{\text{measured}}/\sigma$). S_{measured} and σ are the measured flux density and noise in the 1.16 mm map, and $S_{\text{deboosted}}$ is the deboosted flux density calculated with Eq. 3. The AzTEC ID is from Perera et al. (2008), the MAMBO ID is from Greve et al. (2008).

where S_{bin} is the stacked flux density of N_{bin} sources in a bin of 24 μm flux density or redshift, and $S_{\text{i},1.16}$ and $\sigma_{\text{i},1.16}$ are the measured 1.16 mm flux density and noise at the position of the i-th 24 μm source. This equation does not include any constant terms (w's) because the goal of stacking is to get an average flux density for all sources from a map at one wavelength. The noise decreases with the inclusion of more sources:

$$\sigma_{\text{bin}} = \frac{1}{\sqrt{\sum_{i=1}^{N_{\text{bin}}} \frac{1}{\sigma_{i,1.16}^2}}}. \tag{5}$$

In a mathematical sense, this equation is only valid when all of the $\sigma_{\text{i},1.16}$ are independent; because there are many

24 μm sources in the area of one PSF, this requirement is strictly not met. We fit a Gaussian to the distribution of stacked flux densities for 2484 random pixels, and the σ is the same as the σ_{bin} we calculate for the 24 μm sources using Eq. 5. We choose $N_{\text{bin}} \sim 220$ sources when binning by 24 μm flux density, and $N_{\text{bin}} \sim 660$ sources when binning by redshift. These numbers allow adequate SNR for the stacked flux density in each bin; the redshift bins are larger because we want a differential contribution from the sources in each bin of redshift, whereas we want a cumulative contribution from the sources in each bin of flux density. The contribution to the 1.16 mm background from each bin is $N_{\text{bin}} S_{\text{bin}}/A$, where A is the area. The overlap between the 1.16 mm map

area with $1\sigma < 1$ mJy and the $24\,\mu$m exposure map defines A (0.068 deg^2).

3.1   The effects of angular clustering on stacking analyses

The undetected mm emission from a $24\,\mu$m source covers the area of the mm PSF, so a natural question to ask is: 'What happens to the stacked mm flux density when there are multiple $24\,\mu$m sources in the area encompassed by one mm PSF?' We revisit the fundamental properties of the mm maps to answer this question.

Consider a randomly distributed population of sources. We are interested in the best estimate of the mm flux density of source A, a source with many neighbours. We remember that 0 mJy is the most likely flux density of a randomly chosen pixel; an equivalent statement is that the total flux at the position of A from all of A's randomly distributed neighbors is 0 mJy. To rephrase qualitatively, there are a few neighbours with angular separations small enough to contribute positive flux density at the position of A, but there are many more neighbours with angular separations that are large enough to contribute negative flux density at the position of A. *If we have randomly distributed sources in the area covered by the mm PSF, the true flux densities of the sources are the measured flux densities in the mm map.* Marsden et al. (2009) prove that in the case of randomly distributed sources, stacking is a measure of the covariance between the stacked catalogue and the (sub)mm map.

Let us also consider a population of sources that is *not* randomly distributed – a population that is angularly clustered (as we expect the $24\,\mu$m sources to be). If the clustering is significant at angular separations where the PSF is positive, and if it is negligible at larger angular separations, the positive contribution at the position of A from the many sources that have small angular separations is not cancelled out by the negative contribution from the sources that have large angular separations. In this case, the measured flux density of A is higher than the true flux density – and thus, we cannot blindly stack multiple sources in the same PSF area. The stacked flux density of angularly clustered sources near secure detections is overestimated for the same reason. The ratio of the measured flux densities to the true flux densities for an ensemble of sources is a function of the angular clustering strength of the sources, the flux densities at the wavelength we stack at, and the size of the PSF. We detail our simulation to compute this ratio for the $24\,\mu$m sources and the (sub)mm PSF in §3.2. We further consider the angular clustering of sources with secure (sub)mm detections; the tests we perform suggest that this angular clustering is the dominant source of overestimating the stacked flux density.

The aim of the next section is to investigate the impact of angular clustering on the the stacked (sub)mm flux densities of $24\,\mu$m sources. Using a similar analysis, Chary & Pope (2010) conclude that clustering leads to a significant overestimate of the flux density when stacking on BLAST (sub)mm maps with larger PSFs than those for the SCUBA $850\,\mu$m and 1.16 mm maps.

The angular clustering of $24\,\mu$m sources is uncertain, though spatial clustering measurements exist (Gilli et al. 2007). The assumption we test is that this spatial (three dimensional) clustering projects to an angular (two dimen-

sional) clustering, which may lead to an overestimate of the stacked flux density.

3.2   Quantifying the effects of angular clustering

The two tests of our assertion of angular clustering are:

(1) An estimate of the ratio of measured flux densities to true flux densities for a simulated map composed solely of $24\,\mu$m sources. This test quantifies the effect of angular clustering of $24\,\mu$m sources in the area of one PSF. Here, *true* flux density is an input flux density, and *measured* flux density is an output flux density (after the simulation).

(2) A comparison of the resolved background from stacking on a cleaned map with the resolved background from stacking on a full map. This test helps address the effect of angular clustering of $24\,\mu$m sources with secure (sub)mm detections.

Both tests require a well-characterized PSF: for the first, in order to create a realistic simulated map, and for the second, in order to subtract the secure (sub)mm detections to create a clean map. The 1.16 mm map does not have a well-characterized PSF, so we perform the tests for the Perera et al. (2008) AzTEC 1.1 mm map, with an area defined by $1\sigma < 1$ mJy (0.070 deg^2). We also run the tests for the SCUBA $850\,\mu$m map, with an area defined by $1\sigma < 5$ mJy (0.031 deg^2).

3.2.1   The first test

Our first test is a simulation of an AzTEC 1.1 mm map composed exclusively of $24\,\mu$m sources. Using the relation between $24\,\mu$m flux density and stacked 1.1 mm flux density (the differential form of Fig. 7), we insert best estimates of the 1.1 mm flux densities at the positions of all the $24\,\mu$m sources. This process preserves the angular clustering of the real $24\,\mu$m sources. We then convolve the simulated map with the AzTEC PSF, and remeasure the 1.1 mm flux densities (by stacking). The stacked flux density, multiplied by the number of sources, is the *measured* flux density of the entire sample, while the *true* flux density is the sum of the inserted flux densities. The ratio of total measured flux density to total true flux density is ~ 1.08. Due to angular clustering of multiple sources within the average PSF, the stacked 1.1 mm flux density of $24\,\mu$m sources appears to be overestimated by ~ 8 per cent. Different relations between $24\,\mu$m flux density and 1.1 mm flux density that are physically motivated (for example, from Chary & Elbaz 2001) produce comparable ratios. This 8 per cent correction to the stacked 1.1 mm flux density is within the uncertainties (for example, from the relation between $24\,\mu$m and 1.1 mm flux densities).

An alternative test to the one just presented is an extension of the deblending method in Greve et al. (2010) and Kurczynski & Gawiser (2010). Deblending is the simultaneous solution of a system of Q equations that are mathematical descriptions of the flux densities of blended, angularly clustered sources (Q is the number of sources to be stacked, see §5.2 and fig. 5 in Greve et al. 2010). The result of deblending is a vector of the true source flux densities. Our extension of the methods in Greve et al. (2010) and

Kurczynski & Gawiser (2010) generalizes the equations by not assuming a Gaussian PSF – which does not have the negative parts that are important for the data we consider here – but instead uses the AzTEC PSF for deblending the sources in the AzTEC map. Our extension does not account for $24\,\mu$m undetected sources that may affect the stacked $1.1\,$mm flux of $24\,\mu$m sources. This deblending procedure gives the same answer as our simulations: an 8 per cent overestimation of the stacked $1.1\,$mm flux density.

3.2.2 The second test

Our procedure for cleaning the raw AzTEC $1.1\,$mm map is: 1) for each secure $1.1\,$mm detection, scale the PSF to the deboosted flux density; 2) subtract the scaled PSFs from the raw map; and 3) convolve the residual map with the PSF. There are two components to the resolved $1.1\,$mm background: the contribution to the background from stacking $24\,\mu$m sources, and the contribution to the background from the secure $1.1\,$mm detections cleaned from the map. The latter is calculated by summing the deboosted flux densities of all the secure detections and dividing by the area.

We compare the $1.1\,$mm background resolved from stacking on the full and cleaned maps in Fig. 5 (values in Table 2). A stack of $24\,\mu$m sources on the full map, when compared to a stack on the cleaned map, does *not* significantly overestimate the resolved $1.1\,$mm background.

Fig. 5 implies the clustering of $24\,\mu$m sources with the secure detections in the $1.16\,$mm map will have a small effect on the stacked flux density, although we note that the combined $1.16\,$mm map does have more secure detections (in a larger area with $1\sigma < 1\,$mJy) than the AzTEC $1.1\,$mm map.

The cleaned $850\,\mu$m map is from Pope et al. (2005). We compare the $850\,\mu$m background resolved from stacking on the full and cleaned maps in Fig. 6. The blue diamonds (values in Table 2) show that a stack of $24\,\mu$m sources on the full $850\,\mu$m map overestimates the resolved submm background, when compared to a stack on the cleaned map. We hesitate to attribute the entire difference to angular clustering of $24\,\mu$m sources with the secure $850\,\mu$m detections; the difference is probably due to many effects:

(1) Over-subtraction of the secure $850\,\mu$m detections in making the cleaned map. Detections are subtracted using measured, rather than deboosted, flux densities. To estimate the magnitude of this over-subtraction we clean the raw AzTEC $1.1\,$mm map using both measured and deboosted flux densities for the secure $1.1\,$mm detections, and find a marginal difference in the resolved $1.1\,$mm background between the two methods. The average deboosting correction – roughly 30% of the measured flux subtracted off (Perera et al. 2008; Pope et al. 2006) – is similar for both the $850\,\mu$m and $1.1\,$mm detections; combined with the marginal difference in resolved $1.1\,$mm background, these suggest that the resolved $850\,\mu$m background is insensitive to the over-subtraction of the secure $850\,\mu$m detections in the cleaned map.

(2) Over-subtraction of the secure $850\,\mu$m detections in regions of the map close to the confusion limit. The measured and deboosted flux densities of the detections in the deepest parts of the $850\,\mu$m map are not corrected for the contribution from blended sources below the detection limit.
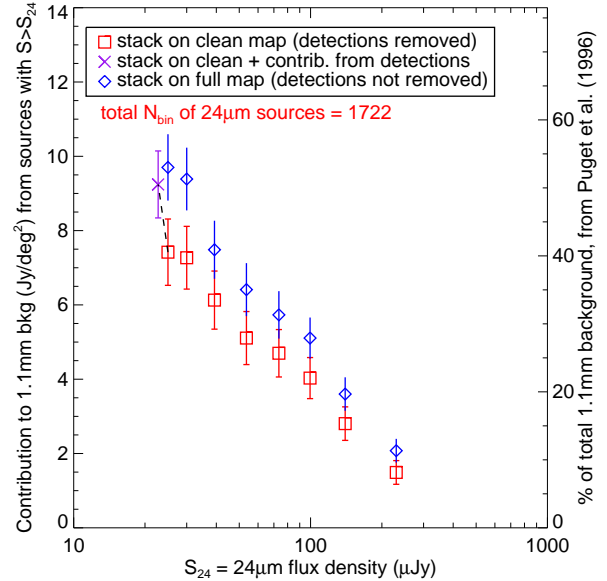

Figure 5. The resolved $1.1\,$mm background from $24\,\mu$m sources with flux densities $> S_{24}$. The red squares are a stack on the cleaned map; the blue triangles are a stack on the full map. The purple 'X' includes the contribution to the background from the secure $1.1\,$mm detections, arbitrarily added to the faintest cumulative flux density bin, after stacking on the cleaned map. Angular clustering of $24\,\mu$m sources with secure $1.1\,$mm detections does not appear to cause a significant overestimate of the resolved $1.1\,$mm background.

We compare the background resolved from stacking on the full and cleaned maps again, this time excluding regions around all detections with $1\sigma < 1\,$mJy; a large difference in the resolved background remains.

(3) Non-uniform noise, which complicates interpretation of the results from the inverse-variance weighted stacking formula.

(4) Different chop throws across the SCUBA map, which complicates the angular separations where we expect to see negative emission from detections.

(5) Angular clustering of the $24\,\mu$m sources with the secure $850\,\mu$m detections.

A simulation of the $850\,\mu$m map, similar to our first test except using *randomly distributed* sources drawn from a differential counts distribution $(\mathrm{d}N/\mathrm{d}S)$ and an idealized SCUBA PSF, implies that part of the difference may be due to effects other than angular clustering (for example, effects 1–4). If this simulation is correct, the stacked $850\,\mu$m flux density is *underestimated* when using the cleaned map, and our estimate of the resolved $850\,\mu$m background is a lower limit. However, the ratio of stacked $850\,\mu$m to $1.16\,$mm flux density as a function of redshift (using the full $850\,\mu$m map) requires a model SED with a higher temperature than $60\,$K (assuming an emissivity index β of 1.5). We therefore use the $850\,\mu$m flux density from stacking on the cleaned map. With large, uniform maps from SCUBA-2 these issues can be tested and resolved – until we have such maps, we cannot separate the effects of angular clustering and non-uniform noise.
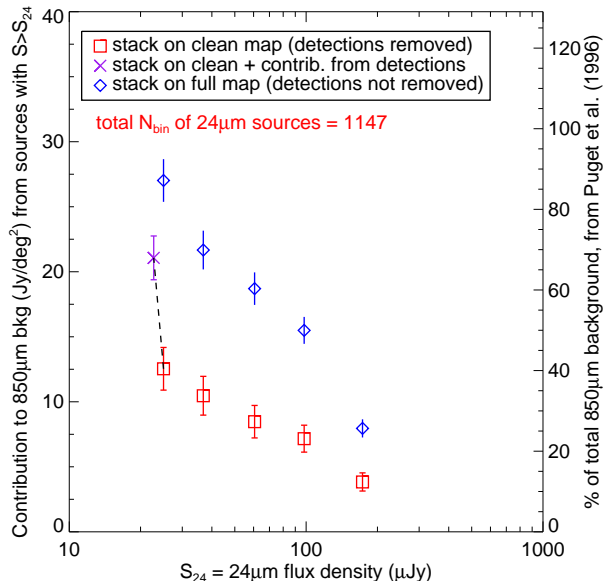
In conclusion, we find that:

Figure 6. The resolved $850\,\mu m$ background from $24\,\mu m$ sources with flux densities $> S_{24}$. The red squares are a stack on the cleaned map; the blue diamonds are a stack on the full map. The purple 'X' includes the contribution to the background from the secure $850\,\mu m$ detections, arbitrarily added to the faintest cumulative flux density bin, after stacking on the cleaned map. In reality, the $24\,\mu m$ counterparts to the secure $850\,\mu m$ detections have flux densities ranging from $S_{24} \sim 20 - 700\,\mu Jy$ (Pope et al. 2006). We adopt the background values from stacking on the cleaned map.

Table 2. A comparison of the resolved background at $850\,\mu m$ and 1.1 mm using SCUBA and AzTEC maps (full and cleaned).

Map	$850\,\mu m$ bkg $\mathrm{Jy\,deg^{-2}}$	1.1 mm bkg $\mathrm{Jy\,deg^{-2}}$
Full	27.0 ± 1.6	9.7 ± 0.9
Cleaned	12.5 ± 1.6	7.4 ± 0.9
Cleaned w/detections	21.1 ± 1.7	9.2 ± 0.9

(1) In the specific case of the $24\,\mu m$ sources and the 1.16 mm map and its PSF, the effects due to angular clustering are additional corrections within the statistical uncertainty of the stacked flux density.

(2) We cannot separate the effect of angular clustering from the effect of non-uniform noise in the SCUBA $850\,\mu m$ map.

The results we present in §4 use the cleaned $850\,\mu m$ map (with the contribution from the secure $850\,\mu m$ detections added after stacking) and the full 1.16 mm map.

4 RESULTS AND DISCUSSION

The stacked 1.16 mm flux density as a function of cumulative $24\,\mu m$ source flux density is shown in Fig. 7. This provides another validation of our method of combining the AzTEC 1.1 mm and MAMBO 1.2 mm maps; the combined 1.16 mm map values (blue diamonds) lie between the stacked flux
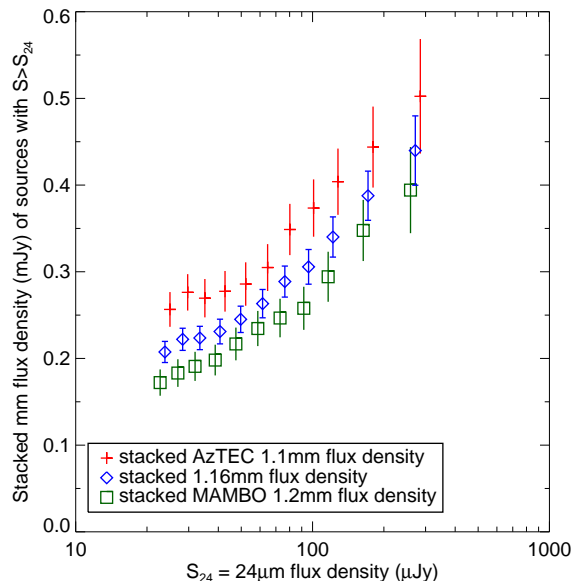

Figure 7. Stacked AzTEC 1.1 mm, combined 1.16 mm, and MAMBO 1.2 mm flux densities from $24\,\mu m$ sources with flux densities $> S_{24}$. The stacked 1.1 mm flux densities are higher than the stacked 1.2 mm flux densities, as expected for the SED of a typical dusty galaxy. The 1.16 mm flux density lies between and has smaller errors than the 1.1 mm and 1.2 mm flux densities.

densities for the individual maps. The stack on the combined 1.16 mm map has smaller errors than the stacks on the individual maps, as anticipated from Eq. 2.

We multiply the stacked flux density (Fig. 7) by the number of $24\,\mu m$ sources in the cumulative bin and divide by the area to get the contribution to the background (Fig. 8). The overlap between the 1.16 mm map area with $1\sigma < 1$ mJy and the $24\,\mu m$ exposure map defines A (0.068 deg^2). The blue diamonds show that $24\,\mu m$ sources resolve $7.6 \pm 0.4\,\mathrm{Jy\,deg^{-2}}$ of the 1.16 mm background.

The total CIB at (sub)mm wavelengths is uncertain due to large scale variability of cirrus emission in the Galaxy that must be subtracted from the observed background, which is measured using *COBE* maps. At 1.16 mm, the published estimates for the total background are $16.4\,\mathrm{Jy\,deg^{-2}}$ (Puget et al. 1996) and $22.0\,\mathrm{Jy\,deg^{-2}}$ (Fixsen et al. 1998) (Table 3).

The left panel in Fig. 9 shows the resolved 1.16 mm background decomposed into redshift bins. Photometric redshift errors for individual $24\,\mu m$ sources should be negligible in bins of this size. The highest redshift bin is for all sources with $z > 1.33$, but we plot it out to $z = 3$ for clarity. We assume that any $24\,\mu m$ sources that fail to match to unique sources with redshift estimates (either spectroscopic or photometric) lie at $z > 1.3$, and we add their contribution to the highest redshift bin.

The 1.16 mm background is not fully resolved by $24\,\mu m$ sources with $S_{24} > 25\,\mu Jy$; most of the portion that is resolved comes from galaxies at high redshift ($z > 1.3$). We repeat our stacking analysis on the cleaned $850\,\mu m$ map to investigate the differences in the resolved portions of the background at $850\,\mu m$ and 1.16 mm.
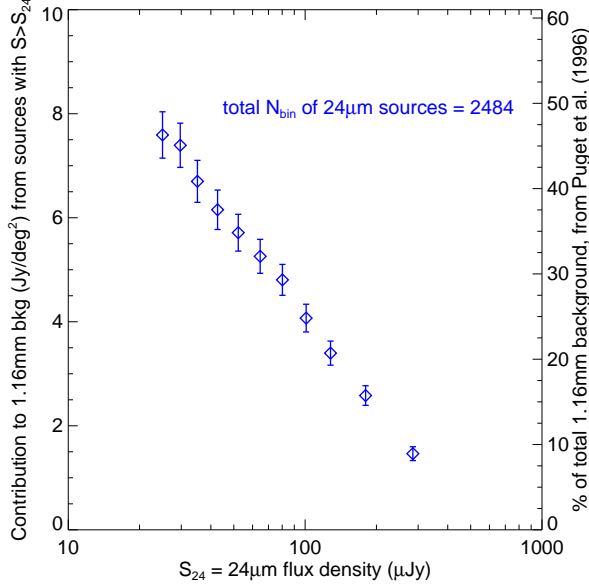
We use the same redshift bins as in the 1.16 mm anal-

Figure 8. Contribution to the 1.16 mm background from 24 μm sources with flux densities $> S_{24}$.

Table 3. The total background at 4 wavelengths.

Wavelength mm	Puget 96 Jy deg^{-2}	Fixsen 98 Jy deg^{-2}	Adopted Jy deg^{-2}
0.85	31	44^{+5}_{-8}	40 ± 9
1.1	18.3	$24.8^{+1.7}_{-4.0}$	$\ldots$
1.16	16.4	$22.0^{+1.4}_{-3.4}$	19.9 ± 3.5
1.2	15.4	$20.4^{+1.1}_{-3.0}$	$\ldots$

ysis (the right panel in Fig. 9). At 850 μm, the values for the total background are 31 Jy deg^{-2} (Puget et al. 1996) and 44 Jy deg^{-2} (Fixsen et al. 1998) (Table 3). The contribution from the secure 850 μm detections is added to the contribution derived from stacking the 24 μm sources on the cleaned map; all secure 850 μm detections have 24 μm counterparts, and we assume for simplicity that the detections lie at $z > 1.3$. This assumption is reasonable, since only 4 of the 33 detections appear to lie at $z < 1.3$ (Pope et al. 2006), and these 4 account for < 5 per cent of the contribution from the detections.

Our analysis does not definitively provide the redshift origins of the total 850 μm background, since it is not completely resolved by 24 μm sources. The results suggest that a large fraction of the resolved 850 μm background originates in galaxies at $z > 1.3$. Wang et al. (2006) perform a stacking analysis and conclude that more than half of the background at 850 μm comes from galaxies at low redshifts ($z < 1.5$). Our methodology differs from that of Wang et al. (2006): they stack a near infrared ($H + 3.6\,\mu$m) sample on a full map with the 850 μm detections.

We show that the background at 850 μm and 1.16 mm is only partially resolved. Can we provide any constraints on the redshifts of the galaxies that contribute to the remainder of the 1.16 mm background?

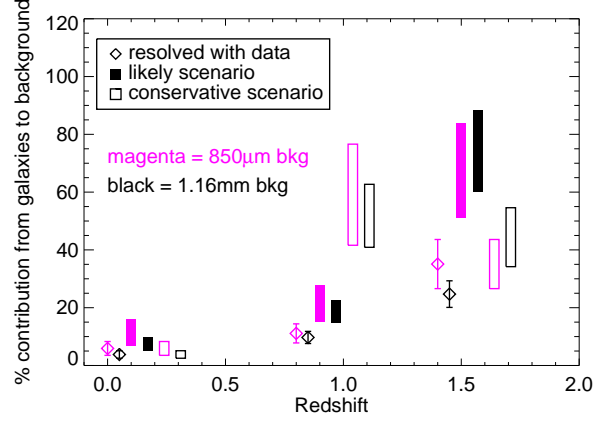There are two often used estimates for the total back-

Figure 10. The redshift origins of the background at 850 μm and 1.16 mm under various scenarios (see §4 for details). The different plotting styles indicate different scenarios; all magenta points/bars are for the 850 μm background, while all black points/bars are for the 1.16 mm background. Points/bars are offset within the redshift bins for clarity. In what we deem the most likely scenario, 60–88 per cent of the 1.16 mm background comes from galaxies at $z > 1.3$.

ground at these two wavelengths. We adopt the average of the range allowed by the two estimates: 19.9 ± 3.5 Jy deg^{-2} at 1.16 mm, and 40 ± 9 Jy deg^{-2} at 850 μm (Table 3). If we assume that the galaxies responsible for the remaining unresolved 850 μm background are distributed to maintain the redshift distribution of the galaxies contributing to the resolved background, then the final decomposition of the 850 μm background is $[z \sim 0.4, z \sim 1, z > 1.3] = [4.5 \pm 1.6$ Jy deg^{-2}, 8.5 ± 1.6 Jy deg^{-2}, 27 ± 2 Jy deg$^{-2}]$. The errors maintain the SNR of the redshift bins of the resolved background. We also assume that the ratios of the resolved 850 μm to 1.16 mm background as a function of redshift (last column of Table 4) hold for the total 850 μm background; we thus convert each contribution to the 850 μm background into an estimate of the contribution to the 1.16 mm background. The decomposition of the 1.16 mm background is thus $4.5/3.1 + 8.5/2.3 + 27/2.9 = 14.4 \pm 0.85$ Jy deg^{-2}. The rest of the 1.16 mm background, which is $19.9 - 14.4 = 5.4 \pm 0.85$ Jy deg^{-2}, presumably comes from galaxies at $z > 1.3$, where the observed submm to mm flux density ratio is lower than the values we use (see, for example, fig. 13 in Greve et al. 2004). The sum of all contributions from galaxies at $z > 1.3$ is 14.8 ± 1.1 Jy deg^{-2}, or 74 ± 14 per cent of the total 1.16 mm background. This likely scenario for the unresolved background is shown with filled bars in Fig. 10.

Although we cannot quantify the probability that the unresolved 850 μm background is distributed as the resolved background, we are able to derive a lower limit to the amount of the total 1.16 mm background that comes from galaxies at $z > 1.3$. In a conservative scenario, all of the remaining unresolved 850 μm background comes from galaxies at $z < 1.3$. Assuming the ratio of 2.3 at $z \sim 1$ holds for the total background, an additional contribution of $40 - 2.3 - 4.4 - 14 = 19.3$ Jy deg^{-2} at 850 μm corresponds to an additional contribution of 8.4 Jy deg^{-2} at 1.16 mm. If the unresolved 850 μm background is produced only by $z < 1.3$ galaxies, the contribution to the 1.16 mm background is
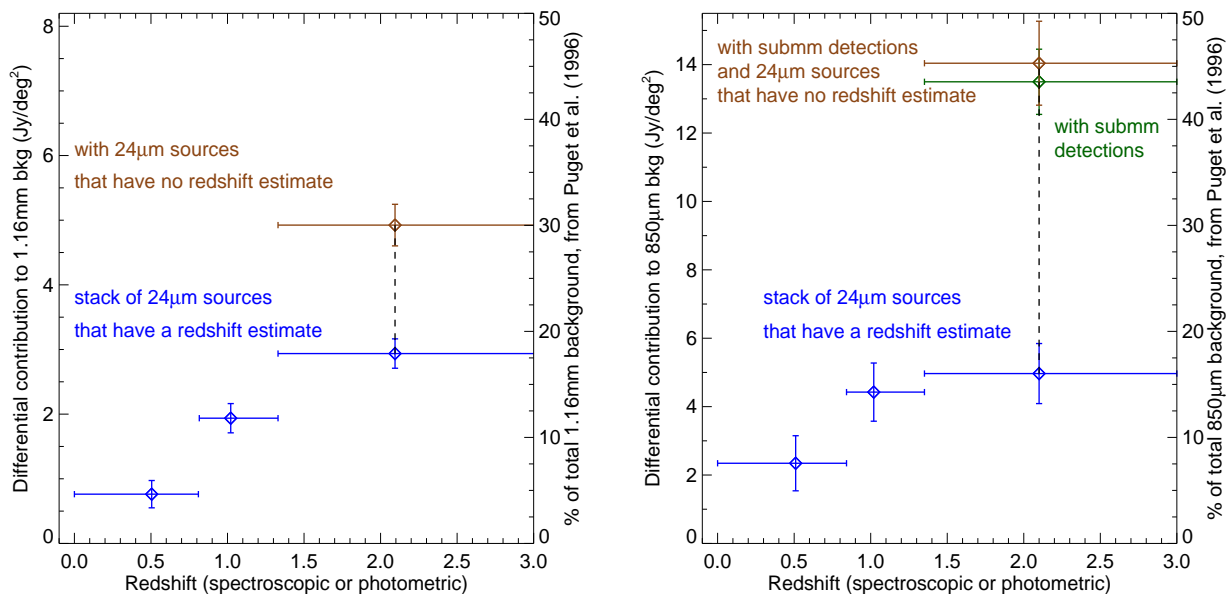
Figure 9. *Left panel*: The (differential) redshift distribution of the resolved 1.16 mm background from 24 μm sources. The diamonds are plotted at the average redshifts of the bins. The brown diamond contains the contributions from the 24 μm sources with $z > 1.3$ and the 24 μm sources without a redshift estimate. *Right panel*: The (differential) redshift distribution of the resolved 850 μm background from 24 μm sources. We use the same redshift bins as in the left panel. The y-axes in both panels show the levels at which the backgrounds are 50 per cent resolved. Most of the resolved background at the two wavelengths comes from galaxies at $z > 1.3$.

Table 4. The redshift distribution of the resolved background at 1.16 mm and 850 μm from 24 μm sources.

z	$S_{\mathrm{bin,1.16}}$ mJy	$N_{\mathrm{bin,1.16}}$	per cent w/spec-z	1.16 mm bkg Jy deg^{-2}	$S_{\mathrm{bin,850}}$ mJy	$N_{\mathrm{bin,850}}$	850 μm bkg Jy deg^{-2}	850/1.16
$0 - 0.82$	0.090 ± 0.025	576	75	0.76 ± 0.21	0.237 ± 0.081	304	2.34 ± 0.81	3.1 ± 1.4
$0.82 - 1.33$	0.199 ± 0.023	660	64	1.94 ± 0.23	0.402 ± 0.077	338	4.42 ± 0.85	2.3 ± 0.5
> 1.33	0.302 ± 0.023	660	26	2.94 ± 0.23	0.492 ± 0.087	310	4.97 ± 0.88	1.7 ± 0.3
with 850 μm detections added to highest z bin								
> 1.33	...	660	...	2.94 ± 0.23	...	343	13.50 ± 0.95	4.6 ± 0.5
with 'redshift unknown' added to highest z bin								
> 1.33	...	1248	...	4.92 ± 0.32	...	538	14.04 ± 1.23	2.9 ± 0.3

Columns: $S_{\mathrm{bin,1.16}}$ is the stacked 1.16 mm flux density of $N_{\mathrm{bin,1.16}}$ sources; $S_{\mathrm{bin,850}}$ is the stacked 850 μm flux density of $N_{\mathrm{bin,850}}$ sources. Column 4 is the percentage of the $N_{\mathrm{bin,1.16}}$ sources that have a redshift determined spectroscopically. Columns 5 and 8 are the resolved background in each bin. Column 9 is the resolved 850 μm background divided by the resolved 1.16 mm background.

$0.8 + 10.3 + 4.9 = 16 \pm 1.3$ Jy deg^{-2}. Again, the remaining $19.9 - 16 = 3.9 \pm 1.3$ of the 1.16 mm background comes from galaxies at $z > 1.3$. At minimum, 44 ± 10 per cent of the total 1.16 mm background comes from galaxies at $z > 1.3$. This conservative scenario is illustrated with unfilled bars in Fig. 10.

An alternate explanation to both scenarios is that all the unresolved background comes from a population of low redshift galaxies with very cold dust and no warm dust (that is, a population of galaxies with a disproportionate amount of large dust grains relative to small dust grains). Our decomposition of the (sub)mm background depends on selecting dusty galaxies at 24 μm – the selection could miss galaxies with little or no warm dust. Galaxies with an excess of cold dust need dust temperatures in the realm of ~ 10 K at $z \sim 1$, and lower temperatures at lower redshifts, to account for the ratio of unresolved 850 μm to 1.1 mm background;

large numbers of galaxies are unlikely to have these extreme dust temperatures.

In this paper, we use observational constraints on the fraction of the (sub)mm background that is resolved to hypothesize that 60–88 per cent of the 1.16 mm background comes from high redshift galaxies. In order to resolve the total 1.16 mm background and provide direct constraints on the redshifts of the galaxies, we need improvements in both the catalogue to be stacked and the mm map. Any stacking catalogue must be deep and homogeneously selected across a large redshift range. The GOODS-N survey at 100 μm with *Herschel* will reach similar (total infrared luminosity) depths as the deepest surveys at 24 μm with *Spitzer*; furthermore, the flux density from 100 μm sources should correlate more tightly with mm flux density than does the flux density from 24 μm sources (dust emitting at 100 μm is a better tracer of the dust emitting at 1 mm). Much deeper radio cat-

alogues than currently exist for stacking, using EVLA and ALMA, are also promising. Alternatively, future large dish (sub)mm telescopes, such as the Large Millimeter Telescope, will provide maps in which the bulk of the galaxies that contribute to the cosmic millimeter background are individually detected. Models presented in Chary & Pope (2010) predict that 60 per cent of the 1.2 mm background comes from galaxies with 1.2 mm flux densities larger than 0.06 mJy (30 times deeper than the combined map).

5 CONCLUSIONS

(1) We create a deep ($\sigma \sim 0.5$ mJy) 1.16 mm map by averaging the AzTEC 1.1 mm and MAMBO 1.2 mm maps in the GOODS-N region. We verify the properties of this map by examining both the deboosted flux densities of the 41 secure detections and the stacked flux density of 24 μm sources. Of the 41 secure detections, 13 are new.

(2) We test the effects of angular clustering of 24 μm sources on the stacked (sub)mm flux density. While clustering does not seem to lead to a significant overestimate of the stacked 1.16 mm flux density, it may be responsible for part of the overestimate of the stacked 850 μm flux density.

(3) 24 μm sources resolve 7.6 Jy deg^{-2} (31–45 per cent) of the 1.16 mm background; 3 Jy deg^{-2} comes from galaxies at $z > 1.3$. 24 μm sources resolve 12.3 Jy deg^{-2} (23–39 per cent) of the 850 μm background, and the submillimeter detections contribute an additional 16–26 per cent; 14 Jy deg^{-2} of the 850 μm background comes from galaxies at $z > 1.3$.

(4) Using the ratio of the resolved 850 μm background to the resolved 1.16 mm background, we propose that 60–88 per cent of the cosmic millimeter background comes from high redshift ($z > 1.3$) galaxies. In the most conservative scenario, 34–55 per cent of the 1.16 mm background comes from galaxies at $z > 1.3$.

We hope to directly detect the majority of the galaxies contributing to the millimeter background with future surveys using large telescopes (for example, the LMT). Deeper catalogues for stacking, at radio and far infrared wavelengths, are needed to fully resolve the mm background. Future studies will also need to assess the effects of angular clustering.

REFERENCES

Barger A. J., Cowie L. L., Wang W.-H., 2008, ApJ, 689, 687

Chary R., Elbaz D., 2001, ApJ, 556, 562

Chary R., Pope A., 2010, ApJ, arXiv:1003.1731

Coppin K., Halpern M., Scott D., Borys C., Chapman S., 2005, MNRAS, 357, 1022

Devlin M. J., et al., 2009, Nature, 458, 737

Dickinson M., Giavalisco M., GOODS Team, 2003, The mass of galaxies at low and high redshift, 324

Dye S., et al., 2006, ApJ, 644, 769

Fixsen D. J., Dwek E., Mather J. C., Bennett C. L., Shafer R. A., 1998, ApJ, 508, 123

Gilli R., et al., 2007, A&A, 475, 83

Gispert R., Lagache G., Puget J. L., 2000, A&A, 360, 1

Greve T. R., Ivison R. J., Bertoldi F., Stevens J. A., Dunlop J. S., Lutz D., Carilli C. L., 2004, MNRAS, 354, 779

Greve T. R., Pope A., Scott D., Ivison R. J., Borys C., Conselice C. J., Bertoldi F., 2008, MNRAS, 389, 1489

Greve T. R., et al., 2010, ApJ, arXiv:0904.0028

Hogg D. W., Turner E. L., 1998, PASP, 110, 727

Kurczynski P., Gawiser E., 2010, AJ, 139, 1592

Lagache G., Puget J.-L., Dole H., 2005, ARA&A, 43, 727

Magnelli B., Elbaz D., Chary R. R., Dickinson M., Le Borgne D., Frayer D. T., Willmer C. N. A., 2009, A&A, 496, 57

Marsden G., et al., 2009, ApJ, 707, 1729

Pascale E., et al., 2009, ApJ, 707, 1740

Perera T. A., et al., 2008, MNRAS, 391, 1227

Pope A., Borys C., Scott D., Conselice C., Dickinson M., Mobasher B., 2005, MNRAS, 358, 149

Pope A., et al., 2006, MNRAS, 370, 1185

Puget J.-L., Abergel A., Bernard J.-P., Boulanger F., Burton W. B., Desert F.-X., Hartmann D., 1996, A&A, 308, L5

Serjeant S., et al., 2008, MNRAS, 386, 1907

Wang W.-H., Cowie L. L., Barger A. J., 2006, ApJ, 647, 74